Supporting information

1. Table S1. A summary of diameter (d) and length (l) of each InAs/InAlAs core shell NW sample investigated in this study

	d (nm)	l (nm)
Length Series	64.3±6.6	1284.4±221.5
	64.5±7.4	1630.2±227.8
	62.1±2.8	2019.4±180.3
	60.6±2.7	2522.2±236.9
Diameter Series	40.6±3.2	1588.4±171.1
	45.5±4.6	1239.0±156.0
	64.5±7.4	1630.2±227.8
	95.2±9.2	1613.0±140.7
	129.8±9.2	2269.6±224.0

2. Absorption measurement

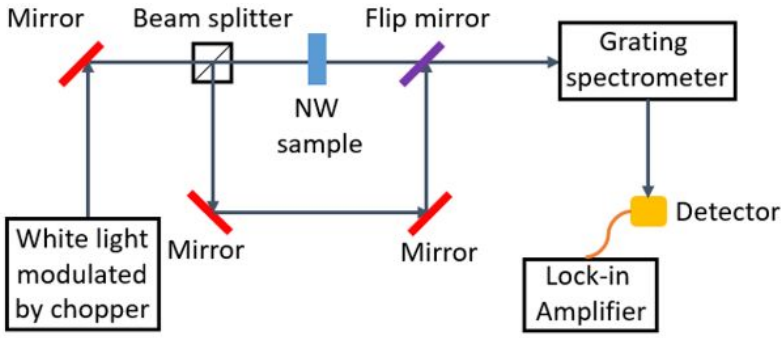

Figure S1. A schematic of the absorption measurement setup.

To determine the amount of incident light absorbed by NWs at the pump wavelength, absorption measurements were performed. A schematic of the setup is shown in Figure S1. A white light bulb was utilized as the broad spectrum light source, which was modulated by a chopper and split into two parts by a beam splitter. A flip mirror in the beam path enabled separate measurements the of samples' reflection (R) and transmission (T). With a spectrometer, R and T spectra were collected by a detector working in conjunction with a lock-in amplifier.

Measurements were conducted on both bare Si (111) substrates and self-catalyzed nanowires grown on Si (111) substrates. Since the Si (111) are undoped, they did not absorb any incident light at pump wavelength 1.3 μm (Figure S2 (a)), and the NWs absorption (A) can be calculated from the reflection (R) and transmission (T) of the NW/Si (111) by A = 1- R-T. Figure S2 (b) shows a representative R and T spectrum of a NW sample (d = 62 nm, l = 2.0 μm) grown on Si (111). The absorption of this NW sample was measured to be 39.0% at 1.3 μm.

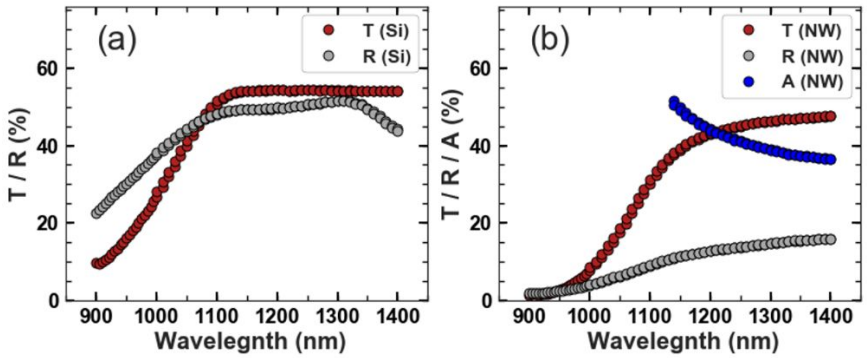

Figure S2. (a) Transmission (T) and reflection (R) spectra of a Si substrate and (b) T, R and absorption (A) spectra of InAs/InAlAs NWs (d = 62 nm, l = 2.0 μm) grown on Si substrate.

Note the $Al_{0.2}In_{0.8}As$ shell is transparent to the pump beam at 1.3 μm. The direct bandgaps (Γ point) of AlAs and InAs are reported to be 3.12eV[1] and 0.415eV[2] at 77K, respectively. Following Vegard's Law, a linear function was adopted to fit the relationship between the bandgap of $Al_xIn_{1-x}As$ alloy and Al concentration x, from which the bandgap energy of the shell is derived to be 0.956 eV (x = 0.2), close to the pump photon energy of 0.953 eV. Moreover, since the absorption at bandedge is low, the $Al_{0.2}In_{0.8}As$ shell was estimated to only absorb a negligible ~1% of the pump beam.

3. Simulation of absorption density distribution within NWs

The light absorption distribution along the NWs at pump wavelength 1.3 μm was studied numerically to check that initial carrier distributions in the NWs were uniform. A series of frequency domain wave optics simulations were performed using COMSOL Multiphysics, finite element analysis approach. Simulations were done on four NW samples in the length series, using a NW diameter of 64nm, length of 1.28μm-2.52μm (InAlAs top segment included), and a fill factor of 3.6%. The simulation area included one NW on the substrate. Periodic boundary conditions were used around the NW to simulate the behavior of a periodic NW array. A normally incident plane wave at the given frequency came from the top (Figure. S3). Then the time-harmonic form of Maxwell's Equations was solved numerically, and the electric and magnetic field distribution obtained in the simulation area. The absorption by the NW was calculated from the field distribution. The Si substrate was assumed to be infinitely thick so the multiple reflections from the Si substrate were neglected. We estimated the contribution from the Si substrate multiple reflections to be less than 1/5 of the first-order absorption. The cross-sectional mapping of the absorption density in a representative NW sample (d=64nm, l=2.02μm) is shown in Figure S3. We define the NW axial direction to be z, and the radial plane to be x-y. Figure S3 (a)-(c) shows the absorption density in the x-z cross section, and (d)-(f) shows the absorption density in the y-z cross section. The integrated absorption density along the x-y plane at each z value for the four investigated NW samples is demonstrated in Figure S4. It can clearly be seen from these figures that the NWs are excited relatively uniformly along the length, with an absorption distribution period of ~650nm.

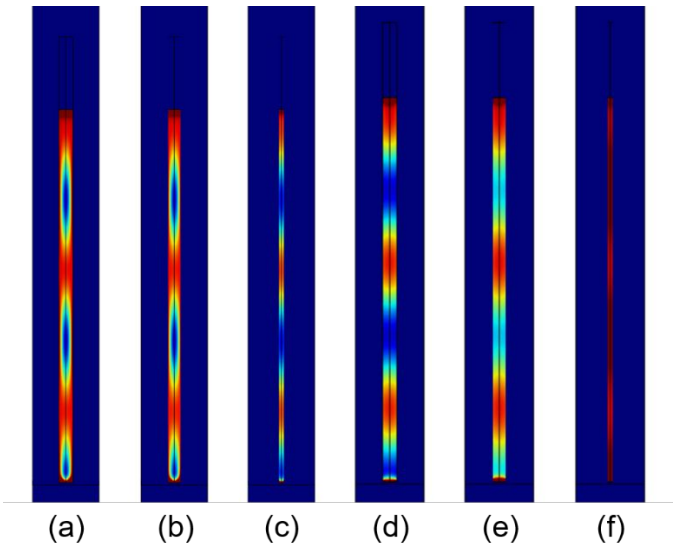

Figure S3. Let $\Delta = 0$ nm denote the cross section that goes through the center of the nanowire. COMSOL simulated absorption density at x-z cross section (a) $\Delta = 0$ nm, (b) $\Delta = 15$ nm (parallel to x-z cross section $\Delta = 0$ nm, 15nm radially outward) and (c) $\Delta = 30$ nm (cross section close to the boundary of NW); absorption density at y-z cross section at (d) $\Delta = 0$ nm, (e) $\Delta = 15$ nm and (f) $\Delta = 30$ nm. The incident light has the electric field along the x direction. Blue (background color) represents zero absorption density.

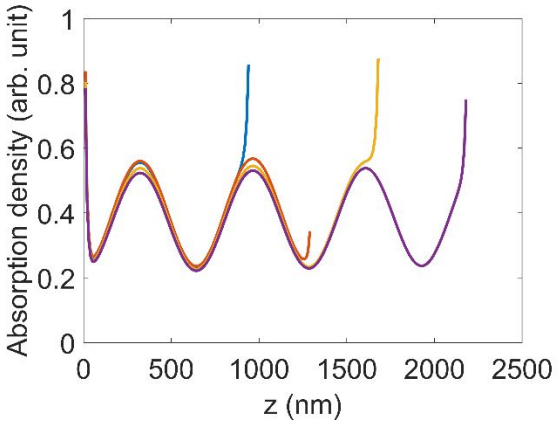

Figure S4. The integrated absorption density along the NW z axis. z=0 is placed at the NW/Si substrate interface. Each curve represents a nanowire of different length, which is indicated by the ending point of the curve.

To gain a picture of the initial spatial redistribution of the carriers, which tends to further smooth the carrier distribution, the electron diffusion rms width σ is estimated. σ can be calculated by $\sqrt{2Dt}$ for a one-dimensional diffusion, where D is the electron diffusion coefficient and $D = \mu^{kT}/e$. Using the InAs NW room temperature electron mobility μ value of 3005 cm^2/Vs (average of 2710, 3300 cm^2/Vs reported by Boland et al.[3],), D is calculated to be 75.87 cm^2/s. The time for an electron to diffuse an rms width σ of 325nm, which is half of the absorption distribution period, is about 7ps.

Given the absorption profile, we can simulate the carrier diffusion by solving the one-dimensional diffusion equation numerically. We assume the carrier concentration is proportional to the

absorption initially. Using a D of 75.87 cm^2/s, the carrier concentration distribution after excitation time t is simulated and shown in Figure S5. It can be seen that the carrier distribution is quite uniform even after ~2ps.

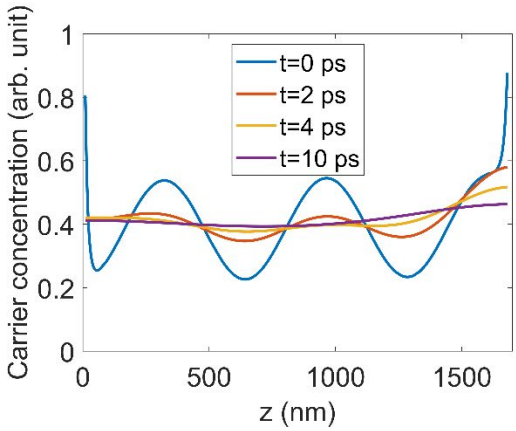

Figure S5. Integrated carrier concentration distribution along NW z-axis after pump excitation time t for a NWs sample (d = 62 nm, l = 2.0 μm).

4. Background carrier density calculations from NW photoluminescence

To evaluate the NW background carrier density, a Fermi-tail fit was applied to the NW photoluminescence (PL) spectrum. This method is suitable for samples which have higher background carrier concentration than the effective density of states (DOS) ~10^{14}cm^{-3} in InAs[4], as successfully demonstrated by Sonner et al.[5] and Lindgren et al.[6] Figure S6 shows the 77K PL of a representative NW sample with d = 130nm, l = 2.3 μm. An 825 nm (1.5 eV) laser diode was used for optical excitation. The pump irradiance on the NW sample was approximately 0.04 mW/μm^2, and pump spot radius 100 μm. Note in Figure S6, the peak position of the nanowire PL emission is around 483meV (2.57μm), which is blue-shifted from the reported emission of zinc-blende planar InAs material (405 meV)[7]. This blueshift is commonly observed in self-catalyzed, wurtzite-phase dominant InAs NWs[5,8,9]. The observed peak energy is close to the PL peak of wurtzite-dominant InAs-InAs$_{0.78}$P$_{0.22}$ core-shell NWs (~488meV) reported by Treu et al.[10], and the PL peak associated with the wurtzite phase segments in the InAs NWs reported by Jurczak et al. (475.6meV in InAs NWs, 491.2 meV in InAs/InP core shell NWs)[11].

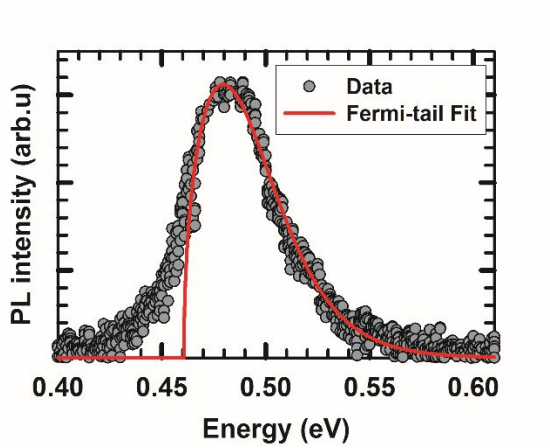

Figure S6. Photoluminescence spectrum of a representative NW sample (d = 130 nm, l = 2.3 μm) at 77K. The red line represents the Fermi-tail fit (on the high energy tail) employed to evaluate the NW background carrier density n.

The carrier concentration n can be expressed as the Fermi-Dirac integral:

$$n(E) = \frac{(2m_{eff} \times e)^{3/2}}{2\pi^2\hbar^3} \int_{Ec}^{\infty} \sqrt{E - E_C} \times \frac{1}{1 + \exp\left(\frac{E - E_f}{kT}\right)} dE \,. \qquad \text{(S1)}$$

The integrand, given by the product of the density of states and the Fermi function, is directly proportional to the PL intensity[5,12], in which E are the energies in the PL spectrum, E_C is the conduction band energy, E_f is the Fermi energy, k is the Boltzmann constant and T is the electron temperature. By applying a least square fit of the integrand to the high energy tail of the PL spectrum, depicted as the red line in Figure S6, E_C, E_f and T as fitting parameters were extracted to be 0.461 (± 6.8×10^{-4}) eV, 0.483 (± 3.58×10^{-3}) eV and 197.9 (± 8.3) K, respectively. n was subsequently obtained by numerically solving the integral using the extracted E_C, E_f and T. In the integral ħ is the reduced Planck constant, e is the electron charge. Since all the NW samples were unintentionally doped, the background doping level was assumed to be low enough (~ 10^{17} cm^{-3}) that m_{eff} can be treated as a carrier concentration independent constant[13]. With m_{eff}= 0.027m_0, where m_0 is the free electron mass[14], n was calculated to be 1.14 (±0.67) × 10^{17} cm^{-3}. This result is in good agreement with the carrier concentration obtained by NW field effect transistor (FET) measurement for the undoped InAs NWs[15].

5. SRH dominance of minority recombination rate

To identify the dominant recombination process in InAs/InAlAs NWs, SRH, radiative and Auger recombination are resolved in the NW sample with the largest diameter (d =130 nm, l = 2.3 μm) in the series. In theory, if each process dominates in a different carrier density regime, they can be individually resolved by ultrafast pump-probe measurement. However, in the InAs/InAlAs NWs, because there is no carrier regime where the radiative recombination dominates, as shown in Figure 2(c), an external quantum efficiency (EQE) experiment was independently conducted to determine the radiative B coefficient.

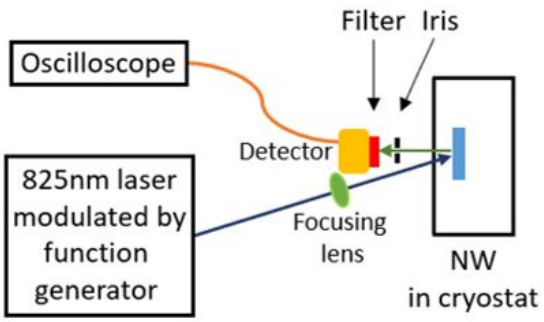

Figure S7. The schematic of EQE measurement setup used in this study.

The schematic of the EQE setup used in this study is shown in Figure S7. The sample was mounted in a liquid nitrogen cooled cryostat for measurement at 77 K. An 825 nm laser diode, which was modulated by a wave function generator, was used for optical excitation. The PL output from the NWs was detected by an InSb detector, which was first placed in front of the cryostat to detect the emission from the front side of the sample, then placed behind the cryostat to detect the emission from the back side of the sample. The detector was used in combination with an oscilloscope, whose peak-to-peak voltage was collected by a computer. To filter out the incident beam as well as PL signal from the substrate, a longpass filter with a cut-on wavelength of 1.65 μm was used in front of the detector. An iris was placed between the sample and the detector, which ensured NW PL from a small solid angle (~10^{-4} sr) was detected. To calculate the integrated PL, we assumed NW output to have a Lambertian distribution, and multiplied the measured PL by π. EQE can be expressed as:

$$EQE = \frac{photons\ out}{photons\ in} = \frac{P_{out}/\frac{hc}{\lambda_{out}}}{P_{in}/\frac{hc}{\lambda_{in}}} \qquad \text{(S2)}$$

where P_{in}, P_{out} are the pump power absorbed by NWs, and PL output power from NWs, respectively, and λ_{in}, λ_{out} are the wavelength of the pump beam and the NW emission, respectively.

The internal quantum efficiency (IQE), which can be extrapolated from EQE, is written as:

$$\text{IQE} = \frac{EQE}{\eta_{ex}} = \frac{B(n_0 + \Delta n)}{R} \qquad \text{(S3)}$$

where η_{ex} is the photon extraction coefficient. The InAs NWs are approximated as an effective layer which has an effective refractive index of $n_1 = n_{air} \times (1 - f) + n_{InAs} \times f$, where n_{InAs} (= 3.51) is the refractive index of InAs bulk layer, f (= 0.04) is the NW fill factor, and n_{air} (= 1) is the index of refraction of vacuum. Since NW PL was detected from both the front and back side of the sample, in place of using the common $n_0^2/4n_1^2$, we used $n_0^2/2n_1^2$ for the extraction coefficient. R is the total recombination rate extracted from pump-probe measurement (Figure 2). As the only unknown variable, B can then be extracted using Eq. S3. Subsequently B can be substituted back into Eq. 3, which can then be fit to the data to obtain the A_{SRH}, and C coefficients.

The main challenge in EQE measurement is that NWs are very prone to heating at higher pump power. This is attributed to the poor thermal conductivity of vacuum as interwire medium, and the small heat sink channel (NW diameter 40-130 nm) between NW and substrate. If heating occurs, the local temperature on the sample will rise, blackbody radiation will ensue, and the NW radiative recombination will be suppressed. Therefore, for pump laser modulation, square waves with various periods and duty cycles generated by the function generator were used to detect interpulse and intrapulse NW heating. By adopting pulses of low duty cycle 1%, 100 μs width, and low input laser power, EQE of the NWs was measured with no heating and no blackbody radiation. Figure S8 shows the IQE of the InAs/InAlAs NWs at 77 K.

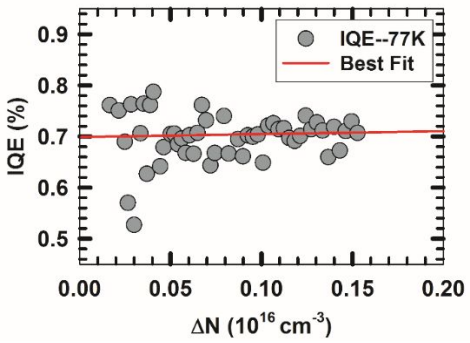

Figure S8. Internal quantum efficiency of a representative NW sample (d = 130 nm, l = 2.3 μm) at 77K.

Using Eq. S3, the radiative coefficient B was extrapolated to be 2.18 $\times 10^{-10}$cm^3/s at 77K from the IQE illustrated in Figure S8. From ultrafast spectroscopy, minority carrier recombination rate R_{MC} ($1/\tau_{MC}$) was measured to be 3.82 ns^{-1} at 77K, and A_{SRH}, C were extrapolated to be 3.76 $\times 10^9$ /s and 1.22×10^{-27}cm^6/s, respectively. With the measured equilibrium background carrier density of 1.14 $\times 10^{17}$cm^{-3}, from Eq. 4, SRH recombination rate is calculated to be 3.76 ns^{-1}, which contributes to 98.4% of R_{MC}. Radiative, Auger recombination rates are 0.0249 ns^{-1}, 0.0159 ns^{-1}, respectively, which are two orders of magnitude smaller than SRH recombination rate. It is obvious that in this measured InAs/InAlAs NW sample, R_{MC} is mainly non-radiative A_{SRH}, which is not only attributed to surface recombination, but also to considerable interior bulk SRH.

The dominance of A_{SRH} in NWs with the largest diameter, therefore the smallest surface-to-volume ratio investigated in this study, suggests that the SRH process would be even more pronounced in NWs with smaller diameters. As temperature increases, SRH recombination rate increases ($A \sim T^{3/2}$), while radiative recombination rate decreases ($B \sim T^{-3/2}$), showing SRH is expected to be more dominant at higher temperatures. We therefore conclude that at all the investigated temperatures, and in all our InAs/InAlAs NW samples, R_{MC} is primarily A_{SRH}.

---

[1] Monemar, B. Fundamental Energy Gaps of AlAs and Alp from Photoluminescence Excitation Spectra. *Phys. Rev. B* **1973**, 8, 5711.
[2] Varshni, Y. P. Temperature Dependence of the Energy Gap in Semiconductors. *Physica* **1967**, 34 (1), 149-154.

[3] Boland, J. L.; Amaduzzi, F.; Sterzl, S.; Potts, H.; Herz, L. M.; i Morral, A. F.; Johnston, M. B. High Electron Mobility and Insights into Temperature-Dependent Scattering Mechanisms in InAsSb Nanowires. *Nano Lett.* **2018**, 18 (6), 3703-3710.

[4] Wirths, S.; Weis, K.; Winden, A.; Sladek, K.; Volk, C.; Alagha, S.; Weirich, T. E.; von der Ahe, M.; Hardtdegen, H.; Lueth, H.; Demarina, N.; Grutzmacher, D.; Schaepers, Th. Effect of Si-Doping on InAs Nanowire Transport and Morphology. *J. Appl. Phys.* **2011**, 110 (5), 053709.

[5] Sonner, M.; Treu, J.; Saller, K.; Riedl, H.; Finley, J. J.; Koblmüller, G. Carrier Concentration Dependent Photoluminescence Properties of Si-Doped InAs. *Appl. Phys. Lett.* **2018**, 112 (9), 091904.

[6] Lindgren, D.; Hultin, O.; Heurlin, M.; Storm, K.; Borgström, M. T.; Samuelson, L.; Gustafsson, A. Study of Carrier Concentration in Single InP Nanowires by Luminescence and Hall Measurements. *Nanotechnology* **2015**, 26 (4), 045705.

[7] IOFFE Institute http://www.io ffe.ru/SVA/NSM/Semicond/InAs/bandstr. html (accessed on May 21, 2019).

[8] Morkötter, S.; Funk, S.; Liang, M.; Döblinger, M.; Hertenberger, S.; Treu, J.; Rudolph, D.; Yadav, A.; Becker, J.; Bichler, M.; Scarpa, G.; Lugli, P.; Zardo, I.; Finley, J. J.; Abstreiter, G.; Koblmüller, G. Role of Microstructure on Optical Properties in High-Uniformity $In_{1-x}Ga_xAs$ Nanowire Arrays: Evidence of a Wider Wurtzite Band Gap. *Phys. Rev. B* **2013**, 87, 205303.

[9] Treu, J.; Speckbacher, M.; Saller, K.; Morkötter, S.; Döblinger, M.; Xu, X.; Riedl, H.; Abstreiter, G.; Finley, J. J.; Koblmüller, G. Widely Tunable Alloy Composition and Crystal Structure in Catalyst-Free InGaAs Nanowire Arrays Grown by Selective Area Molecular Beam Epitaxy. *Appl. Phys. Lett.* **2016**, 108, 053110.

[10] Treu, J.; Bomann, M.; Schmeiduch, H.; Möblinger, M.; Morkötter, S.; Matich, S.; Wiecha, P.; Saller, K.; Mayer, B.; Bichler, M.; Amann, M.-C.; Finley, J. J.; Abstreiter, G.; Koblmüller, G. Enhanced Luminescence Properties of InAs-InAsP Core-Shell Nanowires. *Nano Lett.* **2013**, 13 (2), 6070-6077.

[11] Jurczak, P.; Zhang, Y. Y.; Wu, J.; Sanchez, A. M.; Aagesen, M.; Liu, H. Y. Ten-Fold Enhancement of InAs Nanowire Photoluminescence Emission with an InP Passivation Layer. *Nano Lett.* **2017**, 17 (6), 3629-3633.

[12] Borghs, G.; Bhattacharyya, K.; Deneffe, K.; Van Mieghem, P.; Mertens, R. Band-Gap Narrowing in Highly Doped and P-Type GaAs Studied by Photoluminescence Spectroscopy. *J. Appl. Phys.* **1989**, 66 (9), 4381-4386.

[13] Cardona, M. Electron Effective Masses of InAs and GaAs as a Function of Temperature and Doping. *Phys. Rev.* **1961,** 121 (3), 752−758.

[14] Kim, Y.-S.; Hummer, K.; Kresse, G. Accurate Band Structures and Effective Masses for InP, InAs, and InSb Using Hybrid Functionals. *Phys. Rev. B* 2009, 80 (3), 035203.

[15] Becker, J.; Hill, M. O.; Sonner, M., Treu, J.; Doblinger, M.; Hirler, A.; Riedl, H.; Finley, J. J.; Lauhon, L.; Koblmüller, G. Correlated Chemical and Electrically Active Dopant Analysis in Catalyst-Free Si-Doped InAs Nanowires. *ACS Nano* **2018**, 12 (2), 1603-1610.